Hydrol. Earth Syst. Sci. Discuss., 12, 12215–12246, 2015
www.hydrol-earth-syst-sci-discuss.net/12/12215/2015/
doi:10.5194/hessd-12-12215-2015

Hydrology and Earth System Sciences
Open Access
Discussions

Monitoring infiltration processes with high-resolution surface-based Ground-Penetrating Radar

P. Klenk, S. Jaumann, and K. Roth

Institute of Environmental Physics, Heidelberg University, Im Neuenheimer Feld 229, 69120 Heidelberg, Germany

Received: 6 November 2015 – Accepted: 10 November 2015 – Published: 20 November 2015

Correspondence to: P. Klenk (patrick.klenk@iup.uni-heidelberg.de)

Published by Copernicus Publications on behalf of the European Geosciences Union.

Abstract

In this study, we present a series of high resolution Ground-Penetrating Radar (GPR) measurements monitoring two artificially induced infiltration pulses into two different sands with dual-frequency ground-based GPR. After the application of the second infiltration pulse, the water table in the subsoil was raised by pumping in water from below. The longterm relaxation of the system was then monitored over the course of several weeks. We focused on the capillary fringe reflection and on observed variations in soil water content as derived from direct wave travel times. We discuss the advantages of this dual-frequency approach and show the attainable precision in longterm monitoring of such relaxation processes. Reaching a relative precision of better than 0.001 [–] in water content, we can clearly discern the relaxation of the two investigated sands.

1 Introduction

High-resolution monitoring of soil water flow during infiltration events is a key element in optimizing irrigation procedures or for understanding the dynamics of arid and semi-arid regions. A popular approach with a focus on small scales are dye tracer experiments, which not only visualize the omnipresent soil heterogeneity but in addition highlight phenomena beyond the classical regimes, in particular macropore flow (Kung, 1990; Flury et al., 1994; Perillo et al., 1999; Vervoort et al., 1999; Forrer et al., 2000; Kasteel et al., 2002; Flury and Wai, 2003). Such experiments yield concentration fields with unsurpassed spatial resolution. Furthermore, the tracers can be tuned to the specific transport property of interest. Their major disadvantage comes from limitations in measuring the tracers. There indeed are just two approaches, each with several variants: (i) The soil is excavated, preferably in thin slices, and dye concentration is measured. Apparently, the medium is destroyed afterwards, hence there is just one snapshot. (ii) A glass wall, or tube for that matter, is installed into the soil such that the propagation of the dye can be observed. This propagation is strongly influence by the

HESSD
12, 12215–12246, 2015

wall, however, and it is far from obvious that the observed distribution is at least qualitatively similar to that in the undisturbed soil. At the very least, the depth dimension is lost.

Alternatives are a slew of tomographic and geophysical methods, which are at most minimally invasive and some of which are applicable at scales of a few meters vertically and a few kilometers horizontally. Their typical disadvantages are the reduced spatial resolution and the inability to focus on some particular transport property.

With soil hydrology as the primary interest, Ground-Penetrating Radar (GPR) is a very attractive method as it is non-destructive, highly sensitive to liquid water, provides a useful spatial resolution, and is very fast. As has been repeatedly demonstrated over the past two decades, GPR is especially suited for mapping and monitoring variations in near-surface soil water content (Steelman and Endres, 2012, 2010; Galagedara et al., 2005, 2003; Huisman et al., 2003; Grote et al., 2003; van Overmeeren et al., 1997; Greaves et al., 1996). Therefore, GPR may provide the neccessary means to study soil infiltration processes in a non-destructive manner to great detail. For example, Trinks et al. (2001) imaged an infiltration pulse under well controlled laboratory conditions by a grid of single frequency common offset measurements. Truss et al. (2007) used GPR based observations of infiltrating rainfall as well as artificially induced infiltration into specific geologic structures to decide for a conceptional hydrologic model describing the flowpaths and drainage mechanisms at a oolitic limestone field site. Haarder et al. (2011) mapped different flow phenomena induced by a dye-tracer infused infiltration pulse with GPR and discussed differences betweeen GPR results and infiltration patterns which could be observed from dye distributions after excavating the infiltration plot. Most recently, Allroggen et al. (2015) presented 4-D GPR measurements acquired during a plot scale dye tracer experiment using an automated measurement system on a 2 m × 2 m grid.

All these studies rely on line or grid data acquired by a single offset measurement scheme for interpreting their observations. Mangel et al. (2012) went a step further acquiring automated multi-offset GPR measurements during a spatially distributed in-

HESSD
12, 12215–12246, 2015

filtration experiment applied to a lab-scale sandtank. They used the reflection from the bottom of that tank for monitoring water content variation and compared experimental and modeled results based on hydraulic properties calculated from auxiliary measurements.

Meanwhile a few efforts have also been reported which aim at infering material properties directly based on GPR observations of infiltration events. For example, Moysey (2010) performed a sensitivity analysis of hydrologic trajectories calculated from GPR observations of infiltration into a small sandtank with respect to hydraulic parameters. Using the experimental methodology introduced by Saintenoy et al. (2008); Léger et al. (2014b) estimated the saturated hydraulic conductivity from combining GPR observations of the expansion of an infiltration plume induced directly in the subsurface with numerical modeling. Léger et al. (2014a) calculated a whole set of hydrodynamic parameters for a certain sandy soil based on wetting front reflection travel times recorded when observing water infiltrating with a high-frequency ground-penetrating radar antenna positioned inside a small ring infiltrometer.

Studying soil hydrologic processes quantitatively demands a reliable, reproducible, and precise measurement technique that is highly sensitive to hydraulic observables, which in turn are highly sensitive to the hydraulic aspects of interest. An instance of such aspects are soil hydraulic material properties that are to be estimated.

In this study we focus on the currently attainable precision and resolution both in space and time for monitoring water infiltration into a field-scale test site with GPR. We focus our discussion especially on observing highly sensitive short- and longterm relaxation processes when comparing GPR observations of separate infiltration pulses applied to two different kinds of coarse grained sand.

Secondly, gathering informative data which can be reliably interpreted over a wide range of experimental conditions may be improved by using a multi-common-offset acquisition scheme acquiring data at multiple frequencies, provided this data acquisition can be executed fast enough to capture all relevant phenomena. Therefore, in this study we investigate the efficacy of a novel dual-frequency, multi-channel GPR setup

HESSD
12, 12215–12246, 2015

for 2+1-D monitoring of infiltration pulses while ensuring that coupling enduced signal variation remains minimal.

Finally, our testsite allows to conduct fluctuating water-table experiments in which water is imbibed or drained over the lower boundary. As introduced by Klenk et al. (2015), this enables studying dynamic variations in the capillary fringe reflection. This reflection is due to the permittivity variations occuring in the transition zone above a water table. As a result of an interference phenomenon, it is again highly sensitive to material properties. Expanding on the previous study, we here investigate the long term relaxation time scales of the capillary fringe reflection after being artificially disturbed by imbibition.

2 Material and methods

The experiment and subsequent monitoring measurements presented in this study have been carried out at the ASSESS test site close to Heidelberg. As detailed in (Klenk et al., 2015), the site consists of an artificially built quasi-2-D subsurface structure, featuring three different kinds of sand in differently layered configurations. A corresponding 2-D-sketch along the site's 20 m long main axis is provided in Fig. 1. In contrast to previous studies, the site was not subjected to precipitation but instead decoupled from the environment by adding a greenhouse roof on top about six months prior to the experiments considered here. After this time period, we expect the site to be in hydraulic equilibrium at the start of our experiments.

GPR data were acquired in a common offset (CO) setup moving along the long center axis of the ASSESS site, measuring in a two antenna box setup perpendicularly to the direction of motion. This allows for the measurement to be acquired straight across an infiltration pulse which is administered at the respective locations by a set of commercially available drip irrigation nozzles spread out over a wooden frame with an area of 1 m × 0.2 m and positioned between the two antenna boxes. This setup is shown in the picture in Fig. 2.

HESSD
12, 12215–12246, 2015

We use a ground-based, dual-frequency GPR system manufactured by Ingeneria dei Sistemi (Italy) for data acquisition. Each antenna box contains two transmitters and receivers operating at center frequencies of 200 and 600 MHz, respectively. Data were recorded in an eight channel setup with two internal channels for each frequency measuring right and left of the center line and two cross-box channels measuring at respectively different antenna separations. The sketch in Fig. 4 shows this antenna configuration. As we are only interested in channels monitoring the infiltration pulses for this study, we will restrict ourselves to evaluating the four cross-box channels. We will denote these four channels as CH1 through CH4 throughout this study. Using this nomenclature, CH1 (T1R3) and CH2 (T3R1) are the short and long 600 MHz cross-box channels while CH3 (T2R4) and CH4 (T4R2) denote conversely the respective long and short 200 MHz cross-box channels. The respective antenna separations are also indicated in Fig. 4.

The experiment consisted of three different phases: Two infiltration and one imbibition phases. The forcing is shown in Fig. 3, picturing especially the corresponding water table variation as measured manually in the observation well throughout the whole experiment. Infiltration phases were continued until a quasi-steady state was reached with only small observable variation in the measured GPR data. First, at $t = t_0$ an infiltration pulse was applied along an 1 m long section centered at 6 m while continuously measuring CO data at an antenna box separation of 1.1 m along the middle axis of the site with a temporal resolution of approximately one radargram per minute. During this phase, 0.34 m^3 water were infiltrated over the course of 4 h. One day later, another infiltration pulse was applied to an 1 m long section centered at 12.5 m, which is a location featuring a horizontally layered subsurface structure with a different kind of sand in the top layer. In this case, in total 0.38 m^3 of water were infiltrated over the course of 3.5 h, starting at $t = t_1$. This second infiltration phase was monitored again with an identical CO setup and temporal resolution. Third, immediately after the end of the second infiltration pulse ($t = t_2$), the water table depth was artificially decreased by pumping 6.3 m^3 of water into the observation well which is located at the far end

HESSD
12, 12215–12246, 2015

of the site. This imbibition flux was evenly distributed along the lower boundary of the site by a high-conductivity gravel layer at its bottom and lasted for 3.5 h until $t = t_3$. The minute-resolution GPR data acquisition was stopped after short-time relaxation processes had finished. For investigating longterm relaxation effects, additional GPR CO measurements were executed about once a week for the following three months. All these ensuing monitoring measurements have again been conducted using an identical setup.

We used a temporal sampling rate of 1024 samples over an 80 ns data acquisition window, resulting in a temporal resolution of 1 sample per 0.08 ns on each trace. Data evaluation always included a standard dewow-filter for removing low frequency noise. The amplitude data are then normalized by dividing by a constant factor equal for all radargrams to ensure maximum comparability between measurements. Other than that, only a linearly increasing amplification has been added when plotting radargrams for emphasizing structures arriving at later travel times in plots. As in previous studies (e.g., Gerhards et al., 2008; Klenk et al., 2015), we employ a semi-automated picking algorithm for analyzing travel time variations which follows a center feature of the considered wavelet throughout the course of a radargram.

Direct ground wave travel times can be converted into bulk permittivities ϵ_b [–] based on knowing the respective transmitter-receiver separation and a raypath assumption. Soil water contents θ [–] can be calculated from these permittivity values using the following formulation of the Complex-Refractive Index Model (CRIM, e.g., Birchak et al., 1974):

$$\theta = \frac{1}{\sqrt{\epsilon_w} - 1}\sqrt{\epsilon_b} - \frac{(1-\phi)\sqrt{\epsilon_s} + \phi}{\sqrt{\epsilon_w} - 1}, \quad (1)$$

which represents a linear relationship as a function of $\sqrt{\epsilon_b}$. Equation (1) depends on the soil porosity ϕ [–], the soil matrix permittivity ϵ_s [–] as well as the temperature dependend permittivity of water $\epsilon_w = f(T)$ [–]. Using the physically inspired CRIM as a petrophysical relationship is a critical assumption when propagating the precision

HESSD
12, 12215–12246, 2015

which we obtain in determining permittivities from GPR to water content values (compare, e.g., the discussions about the geometry factor in, Brovelli and Cassiani, 2008). However, for a sandy soil, Eq. (1) usually performs well (e.g., Steelman and Endres, 2011; Roth et al., 1990).

2.1 Results and discussion

First, we evaluate a baseline radargram which was acquired before the start of the actual experiment and illustrates the attainable precision of our setup. Next, the phenomenology of the observed dynamics is introduced based on a series of characteristic radargrams with a specific focus on the capillary fringe relaxation. Then, considering the different signals observed at the center of the second infiltration pulse, the efficacy of our dual-frequency measurements is discussed. Finally, the short and longterm water content variations induced at the two infiltration locations are compared using direct ground wave travel time observations.

A set of three time-lapse movies is available in the supplementary materials of this paper for illustrating the full dynamics which we observe. A corresponding URL can be found at the end of this paper. The first movie shows the temporal evolution of all common offset radargrams recorded by CH2 (600 MHz) and CH4 (200 MHz) during the first infiltration phase. The second movie continues with all radargrams recorded by the same two channels between t_1 and $t_3 + 15.5$ h. Alongside the radargrams, both movies feature time-lapse representations of traces recorded at the two infiltration locations during the experiment. These locations are designated in the radargrams by color-coded arrows. The third movie gives a different perspective by showing the temporal evolution of the radar signal as recorded by CH2 (600 MHz) at every measurement location during the second infiltration event.

HESSD
12, 12215–12246, 2015

2.1.1 Baseline measurement

Figure 5 shows radargrams for all four cross-box channels from a baseline CO measurement acquired before the start of the experiment. Internal structures located above the water table are clearly discernible with a higher spatial resolution achieved by the 600 MHz channels. The well equilibrated condition of the site leads to a well-defined two-featured capillary fringe reflection detectable at arrival times around 22 ns, especially in the first 5 m of the site where the signal is least influenced by interferences with other signals. Decidedly smaller dielectric contrasts in the saturated zone below the water table lead to little reflected energy received at travel times between 25 and 40 ns. At travel times around 40–45 ns, a clear signal is visible originating from the gravel/concrete interface at the bottom of ASSESS site.

The completely dry condition of the topsoil leads to an equally well defined direct wave signal. As there is no water present, observed travel time differences in the direct ground wave signal (compare the dark yellow colored picks drawn in Fig. 5) can directly be associated with variations in the material properties of the different sands. In order to assess the attainable precision of measuring these material differences, the direct wave travel time variation as observed by the four different channels are directly compared in Fig. 6, normalized by the respective antenna separations. To highlight the differences between different materials, the mean travel time for the direct wave measured in sand C is subtracted. The two 600 MHz channels (blue and red lines in Fig. 6) yield very similar results, while there is some variation to be observed between the two 200 MHz channels. These variations may indicate unresolved signals interfering with the respective direct waves, which would especially lead to differences for the 200 MHz results due to their more differing antenna separations (CH3: antenna separation $a = 1.33$ m; CH4: $a = 0.87$ m). Candidate sources for interferences are, e.g., shallow background reflections or antenna ringing due to the rather complicated setup with multiple transmitters and receivers within one shielded antenna box: Refering back

HESSD
12, 12215–12246, 2015

to Fig. 4, the 200 MHz channels' setup is not equivalent with respect to the positioning of the 600 MHz channels' transmitting and receiving antennas.

Hence, relying on the 600 MHz data, we observe travel times in sand B (A) which are consistently about 0.38 (0.12) ns m^{-1} antenna separation larger than in sand C. As the material is completely dry, these travel time variations are solely due to variations in either porosity or soil matrix permittivity. As a quick calculation based on the CRIM shows, rather small variations in either material property can easily account for such a small travel time difference, highlighting the high precision we can achieve. For example, assuming a negligible soil water content and a constant soil matrix permittivity of $\epsilon_s = 5$, the soil porosities we have measured from soil samples ranging between 0.32 ± 0.04 [–] (sand C) and 0.38 ± 0.03 [–] (sand A) would yield a maximum travel time variation of about 0.6 ns. If porosity variations dominated the observed travel time differences, the direct wave velocity should decrease with a decrease in porosity in completely dry conditions. However, comparing, e.g., measured travel times and porosities between sand A and sand B (porosity 0.33 ± 0.02 [–]), this is not the case. Hence, the observed variation is more likely due to differences in ϵ_s [–]. Although $\epsilon_s = 5$ [–] is commonly assumed for most sandy materials, ranges between 4 and 8 have been reported in the literature (e.g., Daniels et al., 2004; Robinson, 2004). Hence, this would allow travel time variations of up to 2 ns for a fixed porosity of $\phi = 0.35$ [–] in dry conditions. In the framework of this study, we cannot disentangle the effect of the two parameters. However, such a baseline measurement under dry conditions allows to base all calculations of water contents on the CRIM in the following form:

$$\begin{aligned}\sqrt{\epsilon_b} &= \sum \theta_i \sqrt{\epsilon_i} \\ &= \theta_w \sqrt{\epsilon_w} + (\phi - \theta_w)\sqrt{\epsilon_a} + (1-\phi)\sqrt{\epsilon_s} \\ &= \theta_w \left(\sqrt{\epsilon_w} - \sqrt{\epsilon_a}\right) + \text{const},\end{aligned} \tag{2}$$

subsuming the impact of material dependent porosity and soil matrix permittivity variations into a constant. This constant can be determined based on the baseline mea-

HESSD
12, 12215–12246, 2015

surement (i.e. $\theta_w = 0$) of the direct ground wave travel time $t_{GW,\,dry}$:

$$\text{const} = \sqrt{\epsilon_b} = \frac{c_0 \cdot t_{GW,\,dry}}{a}, \tag{3}$$

with the antenna separation a and the speed of light in vacuum c_0. Provided our GPR system's time zero can be stabilized appropriately over the course of the experiment, we can even interpret time zero as part of this constant and then rescale increasing direct wave travel time variations measured in infiltration zones directly as increasing water content values:

$$\theta_w = \frac{c_0 \cdot \left(t_{GW,\,curr} - t_{GW,\,dry}\right)}{a \cdot \left(\sqrt{\epsilon_w} - 1\right)}, \tag{4}$$

with the current measured travel time $t_{GW,\,curr}$ and $\sqrt{\epsilon_a} = 1$. Essentially, this approach defines a site and operating system specific calibration based on a single reference measurement of the direct ground wave travel time under completely dry conditions. Hence, in this case we do not need to execute a separate time-zero calibration for calculating soil water content and can therefore avoid antenna-coupling induced uncertainties that are associated with commonly executed air-wave calibration approaches (e.g., Huisman et al., 2003, or Gerhards et al., 2008).

2.1.2 Infiltration/imbibition experiment: phenomenology and capillary fringe behavior

For an overview of the GPR data acquired during the infiltration/imbibition experiment, Fig. 7 showcases a series of 600 MHz common offset radargrams acquired with CH2 at characteristic times of the experiment. These times are indicated in each radargram according to the notation introduced in Fig. 3. The first radargram pictures the state of the system just after the start of the infiltration process at 6.0 m. The second radargram shows the dynamic quasi-steady state 2.25 h into the infiltration process.

HESSD
12, 12215–12246, 2015

Here, the GPR response of the infiltration pulse stays approximately constant, having reached a gravity-flow regime. The increased amount of water in the system would become apparent only by closely monitoring the capillary fringe reflection signal which slowly moves to smaller travel times around the infiltration spot when comparing multiple radargrams (not shown). Radargrams 3 and 4 show the equivalent situations for the second infiltration pulse administered at 12.5 m on the second day. As we will discuss below, the direct wave travel times continuous to increase slowly in this case even after the gravity flow regime has been reached. Radargrams 5–8 then detail the spatial GPR response during and after imbibition. Of particular interest here is the relaxation behavior of the capillary fringe reflection as highlighted by the black rectangles in those three radargrams.

For better visibility, Fig. 8a shows traces averaged over these marked regions from each radargram with the signals originating from the transition zone above the capillary fringe drawn in thick lines. We find a marked signal directly at the end of the imbibition process, governed by the hydraulic properties of the respective materials (black line). As detailed in Klenk et al. (2015), this signal mainly comprises two dinstinct contributions: One part originates from the kink at the top of the capillary fringe and the other from a dynamically induced second kink at the dry end of the dynamically disturbed transition zone. As the system relaxes, this second contribution slowly decays (red line, from radargram 7), and is basically absent almost four days later (blue line, from radargram 8). After these four days, the transition zone above the capillary fringe seems to be very close to equilibrium, as can be seen by the trace drawn in dashed pink. This trace has been measured another five days after radargram 8, showing a virtually identical result when compared to the previous data acquisition. Figure 8b shows the corresponding result as measured at 200 MHz by CH4. In this case, although the dynamic shape of the capillary fringe reflection is clearly discernible, the capillary fringe response cannot be as reliably separated from the signal originating from the layer boundary directly above the water table during relaxation. This is due to the 200 MHz channels' lower spatial resolution and its wider measurement angle in comparison to

HESSD
12, 12215–12246, 2015

the 600 MHz data. Nevertheless, note again the excellent reproducibility of the last two acquired measurements (blue vs. dashed pink lines). Which center frequency will yield the better result will in general depend heavily on the type of experiment and the specific hydraulic state of the system. The excellent results from the 600 MHz data are in part due to the quite homogeneous initial conditions of the experiment. For example, during similar experiments without the greenhouse roof present, precipitation induced soil water content variations in the top part of the ASSESS structure occasionally lead to substantial interferences impeding especially the interpretation of the higher center frequency data.

2.1.3 Interpreting the observed timelapse evolution

For a more detailed interpretation of the observed signals, it is useful to change the perspective. Figure 9 shows the timelapse variation of the GPR signal starting at time $t = t_1$ for the approximate center of the second infiltration pulse around 12.5 m for all four cross-box channels. This representation was chosen to highlight the dynamics observed at different center frequencies and slightly different angles when measuring through the induced infiltration curtain. Equivalent radargrams can be generated at every point of the recorded GPR profile. A corresponding movie which highlights the rich information contained in this dataset by looping over those timelapse radargrams at every point along the profile is provided in the online supplementary materials to this paper. To aid in interpreting the signals, each timelapse radargram recorded at a specific location as shown in the center of the movie is supplemented by two common offset radargrams: The radargram to the left is measured up to that specific trace location *before* t_1, while the common offset radargram on the right is measured starting from that location *after* t_3.

As indicated in the top left radargram in Fig. 9, we can easily observe the temporal variation of (i) the direct ground wave signal (DGW), (ii) the first layer boundary reflection (FLR), (iii) the infiltration front reflection (IFR), (iv) capillary fringe reflection (CFR) and (v) the reflection from the bottom of the ASSESS structure (BR). Compar-

HESSD
12, 12215–12246, 2015

ing the different radargrams illustrates clearly the advantage of this multi-channel dual frequency setup. For example, DGW and FLR are best separable using the shortest 600 MHz channel (CH1) which is a prerequesite for the quantitative DGW evaluation in the following section. Meanwhile, the bottom reflection is best observable for the shortest 200 MHz channel (CH4), giving access to water content variation averaged over the whole profile. Imaging the IFR on the other hand depends heavily on the specific observation angle. In this case, the most coherent signal from the infiltration front is obtained by CH3 at 200 MHz. For each channel, the CFR becomes a prominent feature as soon as the imbibition is started, leading to the sharpening of the transition zone described above. Comparing different frequencies, we observe the higher resolution of the 600 MHz data which leads to an explicit imaging of interference patterns with subsurface structure reflections which the 200 MHz data do not resolve.

2.1.4 Monitoring infiltration and relaxation in different sands

In order to characterize the infiltration process at the two different locations in more detail, we will now evaluate the travel time variation of the direct ground wave (DGW) signal. As stated above, CH1 is best suited for quantitative evaluation of the DGW signal. Based on the DGW travel time calculated from the initial baseline measurement (i.e. the respective dry state travel times), Fig. 10 shows the water content variation for both infiltration events. The dark solid lines show the results based on a spatial average of all traces contained in ±0.05 m around the center of the infiltration. Increasingly lighter colored lines denote increasing spatial averaging ranges up to a maximum averaging range of ±1.3 m. As expected, this leads to slowly decreasing averaged water contents with increasing the size of the averaging volume. However, the overall small changes testify to the robustness of our approach.

For comparing the results from both infiltration events, the respective curves are shifted to coincide at the end of the respective infiltration period. First, notice the short timescales both at the beginning and at the end of each infiltration event, illustrating the necessity for the high temporal resolution of our measurements. For both infiltration

HESSD
12, 12215–12246, 2015

events, the DGW signal reaches a quasi-steady state (i.e. a gravitational flow regime in the top part of the soil profile) after an initial water content increase by about 0.1 during the first 0.25 h. For the first infiltration event (black line), we observe only a small further water content increase of about 0.01 over the rest of the infiltration period. However, for the second infiltration event (blue line), there is a much larger continued linear increase of about 0.03 until the infiltration was stopped. We attribute this behavior to the interaction of the infiltrating pulse with the different subsurface structures at the two locations. In our particular case (relative hydraulic properties at the first layer interface and the specific forcing) the infiltrating water will pond on the first layer boundary which is a horizontal interface for the location of the second infiltration pulse. In contrast, this is not the case at the first infiltration location, due to slanted reflectors and a different material contrast.

2.1.5 Long-term monitoring

As can be observed from Fig. 10, the initial relaxation behavior of DGW derived water contents for both infiltration events is very similar, with the largest part of the observable dynamics occuring within the first 0.5 h after stopping the infiltration. At later times, these variations stay observable but become increasingly minute. We continued regular CO monitoring measurements at increasing time intervals after the end of the main experiment for almost three months. Figure 11 shows water content variations calculated from the DGW travel time of CH1. At the time of the last measurement (red line), there is an additional peak to be observed around 13.5 m which is due to a hole in the greenhouse roof leading to a new infiltration spot at this location. The figure illustrates that we can reliably resolve water content variations of less than 0.001 based on the DGW travel time with this setup.

Throughout the monitoring period, we consistently observe an increasingly small decrease in water content at the two infiltration locations. Due to the nature of our rather coarse grained sands, even after these three months, the system has not reached its original equilibrium state. This is due to the high non-linear nature of the respective hy-

HESSD
12, 12215–12246, 2015

draulic conductivity functions with increasingly small conductivities in the dry regime. In contrast to the short term processes, the longterm relaxation dynamics exhibits notable differences for both sands. This is shown in Fig. 12, picturing the peak water content relaxation in each case. Note that for the infiltration into sand B, water contents have been calculated from the travel times not observed directly at the center of the infiltration pulse since the section between 6 and 6.3 m is increasingly influenced by an interfering shallow layer reflection for later monitoring measurements. Towards the end of our observation period, the coarser grained sand C (blue line) retains about 0.01 [–] more water than sand B (black line). Despite differing water contents at the start of the relaxation phase, we can conclude that this is due to a comparatively smaller hydraulic conductivity of the coarser material at low water contents. The same relative longterm behavior in the two sands would have been observed for higher initial water content values in sand B. In this case, the black curve would simply show a sharper decrease in water content at the beginning of the relaxation phase before approaching the curve shown here.

3 Conclusions

In this study, we introduce a novel dual-frequency, surface-based multi-channel GPR setup for high-resolution time-lapse monitoring of hydraulic processes. The main focus is monitoring two infiltration pulses which are applied to two different kinds of sand with a different but known subsurface-structure. The availability of two different frequencies, several channels measuring through the imposed infiltration pulses at different antenna separations and a high temporal resolution allows for a reliable interpretation of all observed signals. We find that for the specific hydraulic dynamics induced here, the detailed spatial resolution of the 600 MHz channels allows for a reliable quantitative evaluation of the direct ground wave travel times with a relative precision of less than 0.001 [–] in water content. These water content values can be directly calculated based

HESSD
12, 12215–12246, 2015

on a baseline measurement under completely dry conditions without the need for an additional time-zero calibration measurement.

Furthermore, after additionally raising the water table in the system, the relaxation behavior of the capillary fringe reflection can be studied to great detail based on the high frequency data. In contrast, evaluating signals from deeper layers such as the bottom layer reflection would be more reliable using the lower frequency due to a better signal to noise ratio.

Finally, while the capillary fringe relaxes on a time-scale of a few days, the decaying infiltration induced water content variations can be observed by the direct ground wave consistently over the course of several months. Due to our high precision, notable differences could be observed in the longterm relaxation behavior of the two sands studied here.

The Supplement related to this article is available online at doi:10.5194/hessd-12-12215-2015-supplement.

Acknowledgements. We thank Viktoria Keicher for her invaluable help during data acquisition and Angelika Gassama for technical support operating the ASSESS site. We acknowledge financial support by the Deutsche Forschungsgemeinschaft through project RO 1080/12-1.

References

Allroggen, N., van Schaik, N. L. M., and Tronicke, J.: 4-D ground-penetrating radar during a plot scale dye tracer experiment, J. Appl. Geophys., 118, 139–144, doi:10.1016/j.jappgeo.2015.04.016, 2015. 12217

Birchak, J. R., Gardner, C. G., Hipp, J. E., and Victor, J. M.: High dielectric constant microwave probes for sensing soil moisture, P IEEE, 62, 93–98, doi:10.1109/PROC.1974.9388, 1974. 12221

HESSD

12, 12215–12246, 2015

Brovelli, A. and Cassiani, G.: Effective permittivity of porous media: a critical analysis of the complex refractive index model, Geophys. Prospect., 56, 715–727, doi:10.1111/j.1365-2478.2008.00724.x, 2008. 12222

Daniels, D. J.: Ground Penetrating Radar, the Institution of Electrical Engineers, London, UK, doi:10.1049/PBRA015E, 2004. 12224

Flury, M. and Wai, N. N.: Dyes as tracers for vadose zone hydrology, Rev. Geophys., 41, 1002, doi:10.1029/2001RG000109, 2003. 12216

Flury, M., Flühler, H., Jury, W. A., and Leuenberger, J.: Susceptibility of soils to preferential flow of water: a field study, Water Resour. Res., 30, 1945–1954, doi:10.1029/94WR00871, 1994. 12216

Forrer, I., Papritz, A., Kasteel, R., Flühler, H., and Luca, D.: Quantifying dye tracers in soil profiles by image processing, Eur. J. Soil Sci., 51, 313–322, doi:10.1046/j.1365-2389.2000.00315.x, 2000. 12216

Galagedara, L. W., Parkin, G. W., and Redman, J. D.: An analysis of the ground-penetrating radar direct ground wave method for soil water content measurement, Hydrol. Process., 17, 3615–3628, doi:10.1002/hyp.1351, 2003. 12217

Galagedara, L. W., Parkin, G. W., Redman, J. D., von Bertoldi, P., and Endres, A. L.: Field studies of the GPR ground wave method for estimating soil water content during irrigation and drainage, J. Hydrol., 301, 182–197, doi:10.1016/j.jhydrol.2004.06.031, 2005. 12217

Gerhards, H., Wollschläger, U., Yu, Q., Schiwek, P., Pan, X., and Roth, K.: Continuous and simultaneous measurement of reflector depth and average soil-water content with multi-channel ground-penetrating radar, Geophysics, 73, J15–J23, doi:10.1190/1.2943669, 2008. 12221, 12225

Greaves, R., Lesmes, D., Lee, J., and Toksöz, M.: Velocity variations and water content estimated from multi-offset, ground-penetrating radar, Geophysics, 61, 683–695, doi:10.1190/1.1443996, 1996. 12217

Grote, K., Hubbard, S., and Rubin, Y.: Field-scale estimation of volumetric water content using ground-penetrating radar ground wave techniques, Water Resour. Res., 39, 1321, doi:10.1029/2003WR002045, 2003. 12217

Haarder, E. B., Looms, M. C., Jensen, K. H., and Nielsen, L.: Visualizing unsaturated flow phenomena using high-resolution reflection ground penetrating radar, Vadose Zone J., 10, 84–97, doi:10.2136/vzj2009.0188, 2011. 12217

HESSD
12, 12215–12246, 2015

Huisman, J. A., Hubbard, S. S., Redman, J. D., and Annan, A. P.: Measuring soil water content with ground penetrating radar: a review, Vadose Zone J., 2, 476–491, available at: http://vzj.geoscienceworld.org/cgi/content/abstract/2/4/476 (last access: 6 November 2015), 2003. 12217, 12225

Kasteel, R., Vogel, H. J., and Roth, K.: Effect of non-linear adsorption on the transport behaviour of brilliant blue in a field soil, Eur. J. Soil Sci., 53, 231–240, doi:10.1046/j.1365-2389.2002.00437.x, 2002. 12216

Klenk, P., Jaumann, S., and Roth, K.: Quantitative high-resolution observations of soil water dynamics in a complicated architecture using time-lapse ground-penetrating radar, Hydrol. Earth Syst. Sci., 19, 1125–1139, doi:10.5194/hess-19-1125-2015, 2015. 12219, 12221, 12226, 12235

Kung, K.-J.: Preferential flow in a sandy vadose zone: 1. Field observation, Geoderma, 46, 51–58, doi:10.1016/0016-7061(90)90006-U, 1990. 12216

Léger, E., Saintenoy, A., and Coquet, Y.: Hydrodynamic parameters of a sandy soil determined by ground-penetrating radar inside a single ring infiltrometer, Water Resour. Res., 50, 5459–5474, doi:10.1002/2013WR014226, 2014a. 12218

Léger, E., Saintenoy, A., and Coquet, Y.:Estimating saturated hydraulic conductivity from ground-based GPR monitoring Porchet infiltration in sandy soil, in: Ground Penetrating Radar (GPR), 2014 15th International Conference on 30 June–4 July 2014, Brussels, Belgium, 124–130, doi:10.1109/ICGPR.2014.6970399, 2014b. 12218

Mangel, A. R., Moysey, S. M. J., Ryan, J. C., and Tarbutton, J. A.: Multi-offset ground-penetrating radar imaging of a lab-scale infiltration test, Hydrol. Earth Syst. Sci., 16, 4009–4022, doi:10.5194/hess-16-4009-2012, 2012. 12217

Moysey, S. M.: Hydrologic trajectories in transient ground-penetrating-radar reflection data, Geophysics, 75, WA211–WA219, doi:10.1190/1.3463416, 2010. 12218

Perillo, C. A., Gupta, S. C., Nater, E. A., and F., M. J.: Prevalence and initiation of preferential flow paths in a sandy loam with argillic horizon, Geoderma, 89, 307–331, doi:10.1016/S0016-7061(98)00087-1, 1999. 12216

Robinson, D.: Measurement of the solid dielectric permittivity of clay minerals and granular samples using a time domain reflectometry immersion method, Vadose Zone J., 3, 705–713, 2004. 12224

HESSD
12, 12215–12246, 2015

Roth, K., Schulin, R., Flühler, H., and Attinger, W.: Calibration of time domain reflectometry for water content measurement using a composite dielectric approach, Water Resour. Res., 26, 2267–2273, doi:10.1029/WR026i010p02267, 1990. 12222

Saintenoy, A., Schneider, S., and Tucholka, P.: Evaluating ground penetrating radar use for water infiltration monitoring, Vadose Zone J., 7, 208–214, 2008. 12218

Steelman, C. M. and Endres, A. L.: An examination of direct ground wave soil moisture monitoring over an annual cycle of soil conditions, Water Resour. Res., 46, W11533, doi:10.1029/2009WR008815, 2010. 12217

Steelman, C. M. and Endres, A. L.: Comparison of petrophysical relationships for soil moisture estimation using GPR ground waves, Vadose Zone J., 10, 270–285, doi:10.2136/vzj2010.0040, 2011. 12222

Steelman, C. M. and Endres, A. L.: Assessing vertical soil moisture dynamics using multi-frequency GPR common-midpoint soundings, J. Hydrol., 436–437, 51–66, doi:10.1016/j.jhydrol.2012.02.041, 2012. 12217

Trinks, I., Stümpel, H., and Wachsmuth, D.: Monitoring water flow in the unsaturated zone using georadar, First Break, 19, 679–684, 2001. 12217

Truss, S., Grasmueck, M., Vega, S., and Viggiano, D. A.: Imaging rainfall drainage within the Miami oolitic limestone using high-resolution time-lapse ground-penetrating radar, Water Resour. Res., 43, W03405, doi:10.1029/2005WR004395, 2007. 12217

van Overmeeren, R., Sariowan, S., and Gehrels, J.: Ground penetrating radar for determining volumetric soil water content; results of comparative measurements at two test sites, J. Hydrol., 197, 316–338, doi:10.1016/S0022-1694(96)03244-1, 1997. 12217

Vervoort, R. W., Radcliffe, D. E., and West, L. T.: Soil structure development and preferential solute flow, Water Resour. Res., 35, 913–928, doi:10.1029/98WR02289, 1999. 12216

HESSD
12, 12215–12246, 2015

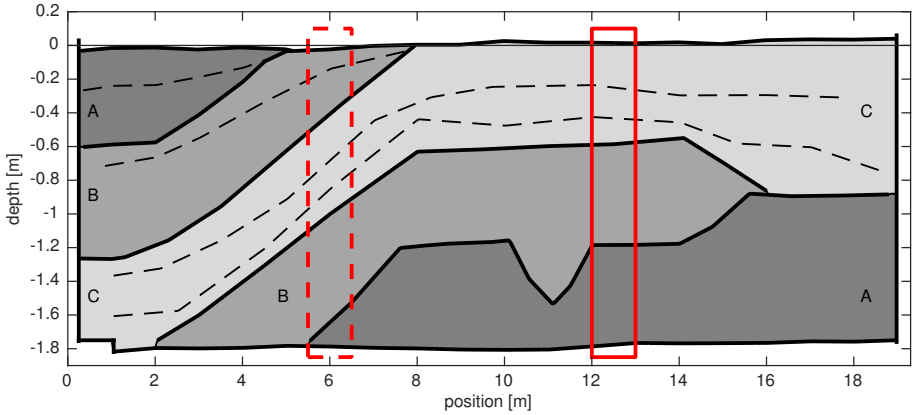

Figure 1. Overview of the subsurface structure of the ASSESS site, featuring three different kinds of sand A, B and C. Dashed lines indicate known compaction layers within the same material, which are an artifact of the building process. The two infiltration spots at 6 and 12.5 m are marked by red rectangles; modified from Klenk et al. (2015).

HESSD
12, 12215–12246, 2015

Figure 2. Measurement setup with the infiltration device. The GPR measurements were taken perpendicularly to the line of motion, across the infiltration curtain.

HESSD
12, 12215–12246, 2015

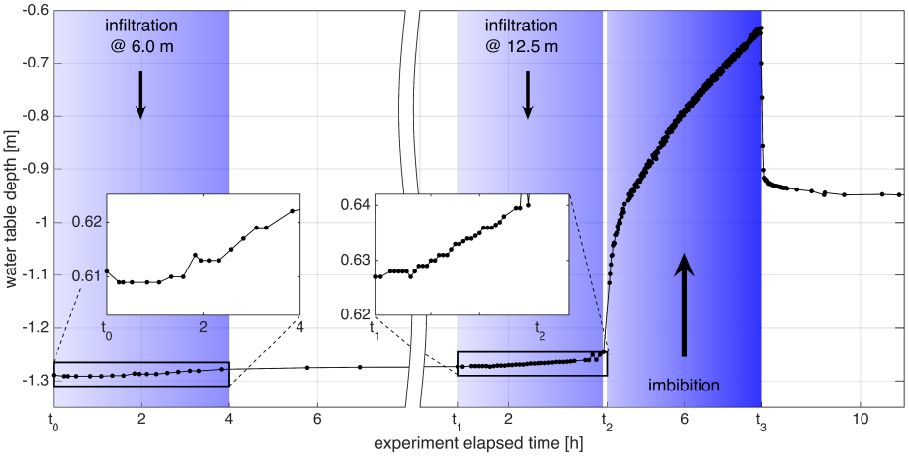

Figure 3. Water table depth as measured manually in the observation well throughout the experiment. The two infiltration phases and the following imbibition phase are marked by the color graded blue boxes. The two insets show an equally magnified view of the small but notable water level increase after the respective infiltration pulses reach the water table.

HESSD
12, 12215–12246, 2015

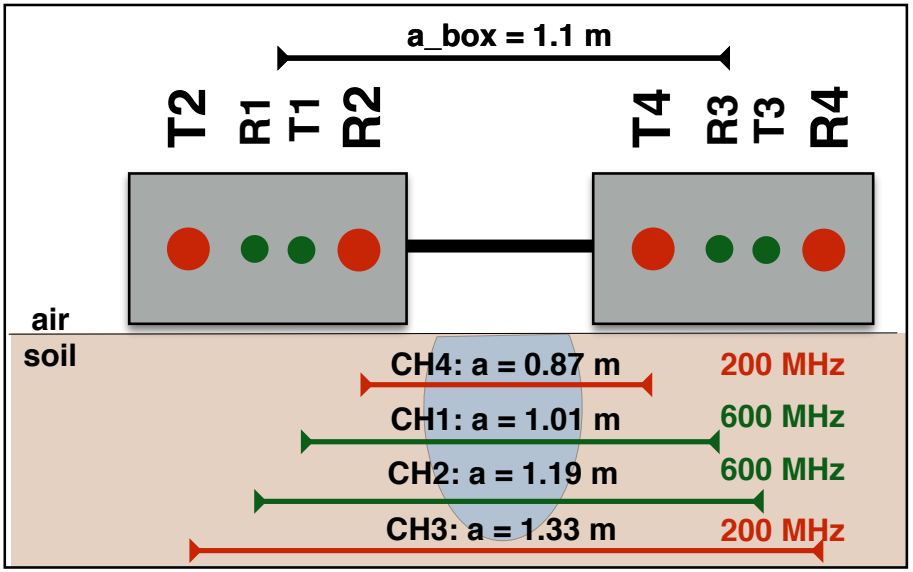

Figure 4. Sketch of the GPR system setup. In this study, we will only evaluate the four cross box channels denoted CH1 through CH4, imaging directly the infiltration pulses applied between the two antennas (see picture in Fig. 2). CH1 (T1R3) and CH2 (T3R1) are the short and long 600 MHz cross-box channels while CH3 (T2R4) and CH4 (T4R2) denote the respective long and short 200 MHz cross-box channels. The direction of motion for common offset data acquisition is perpendicular to the drawing plane.

HESSD
12, 12215–12246, 2015

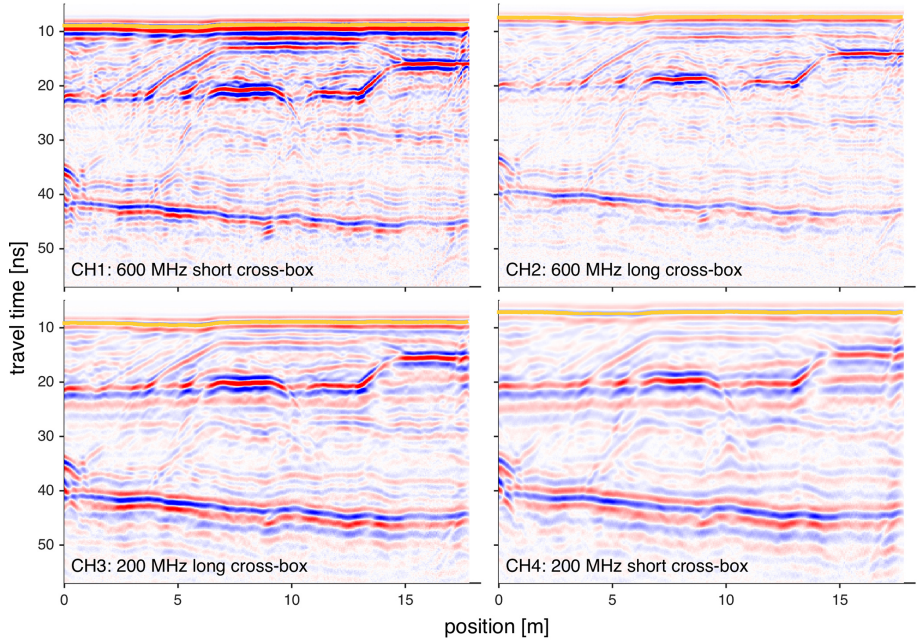

Figure 5. Baseline common offset radargrams of the four crossbox channels acquired before the start of the experiment. Subsurface structures above the water table are well resolved. Note the prominent capillary fringe reflection signal recorded around 22 ns as well as the reflection from the bottom of the structure recorded around 42 ns. For each radargram, the direct wave pick used for comparing measured travel times in Fig. 6 is indicated by a dark yellow line.

HESSD
12, 12215–12246, 2015

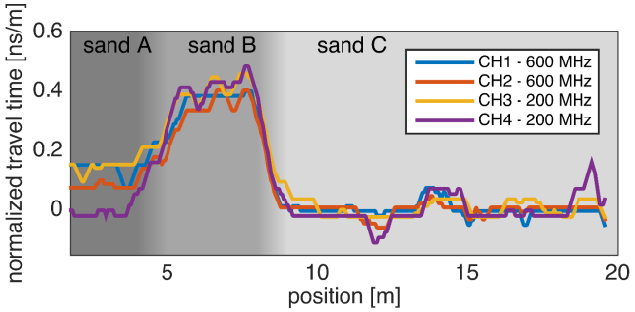

Figure 6. Comparison of the direct wave travel times as evaluated for the four different channels. Travel times have been normalized by the respective antenna separation and the mean travel time of the section between 10 and 18 m has been subtracted as reference. Comparing the sections pertaining to different materials in the top layer, this figure shows that we can reliably resolve material induced travel time differences of approximately 0.1 ns. 600 MHz data agree perfectly, while there is some variation present in 200 MHz data.

HESSD
12, 12215–12246, 2015

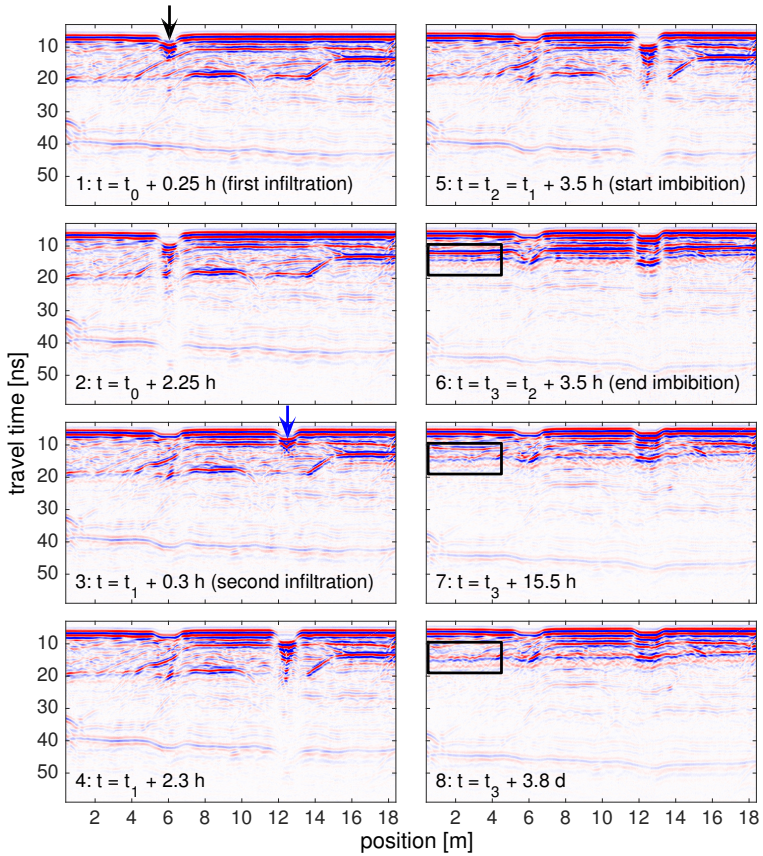

Figure 7. Series of characteristic radargrams measured by CH1 at 600 MHz center frequency illustrating different stages of the experiment. Infiltration events took place at the locations indicated by the black and blue arrows, respectively. The black boxes in radargrams 6–8 are analyzed in more detail in Figs. 8a and b, highlighting the relaxation of the capillary fringe reflection observed over several days.

HESSD
12, 12215–12246, 2015

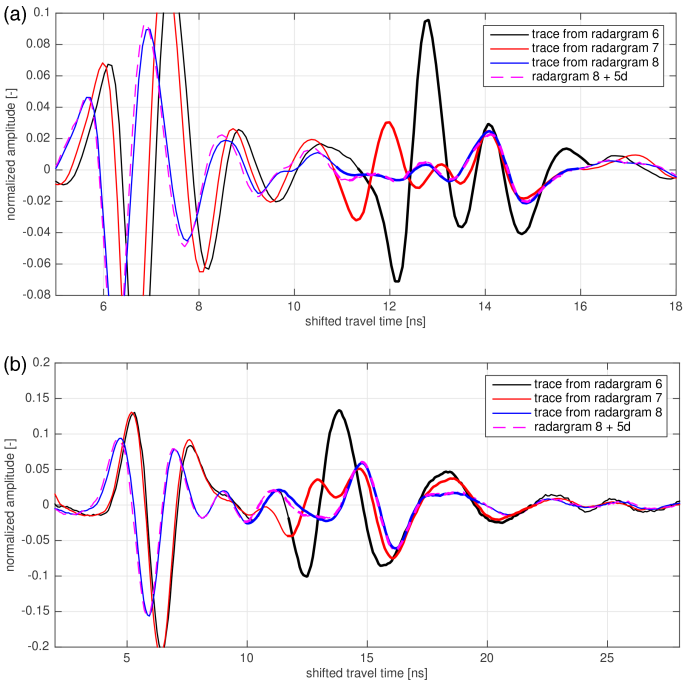

Figure 8. (a) Detailed view of the relaxation of the capillary fringe reflection measured at 600 MHz and averaged over the black rectangles in radargrams 6–8 from Fig. 7. For clarity, the traces have been shifted to coincide at the second maximum feature of the CFR signal at the end of imbibition. Note the disappearance of the signal part between 11 and 12.5 ns between the second day (red line) and the four days later (blue). **(b)** Detailed view of the relaxation of the capillary fringe reflection measured at 200 MHz and averaged over the black rectangles in radargrams 6–8 from Fig. 7. Clearly, the 200 MHz data suffer in this case from interferences of the signal's upper part with a layer reflection above, which the 600 MHz data can resolve directly.

HESSD
12, 12215–12246, 2015

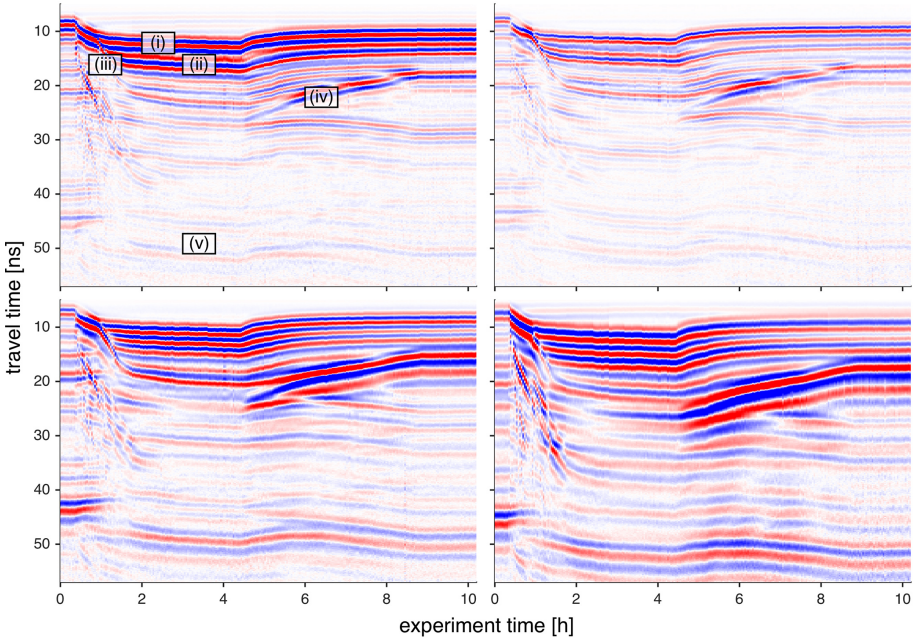

Figure 9. Exemplary time-lapse radargrams for all four crossbox channels, synthesized from all traces measured in the center of the second infiltration spot at 12.5 m during the second experiment phase. The infiltration phase lasted from $t_1 + 0.3$–3.5 h, after which the immediate switch to imbibition took place, stopping at $t_1 + 7$ h. A timelapse movie illustrating the whole experiment is provided in the supplementary materials of this paper.

HESSD
12, 12215–12246, 2015

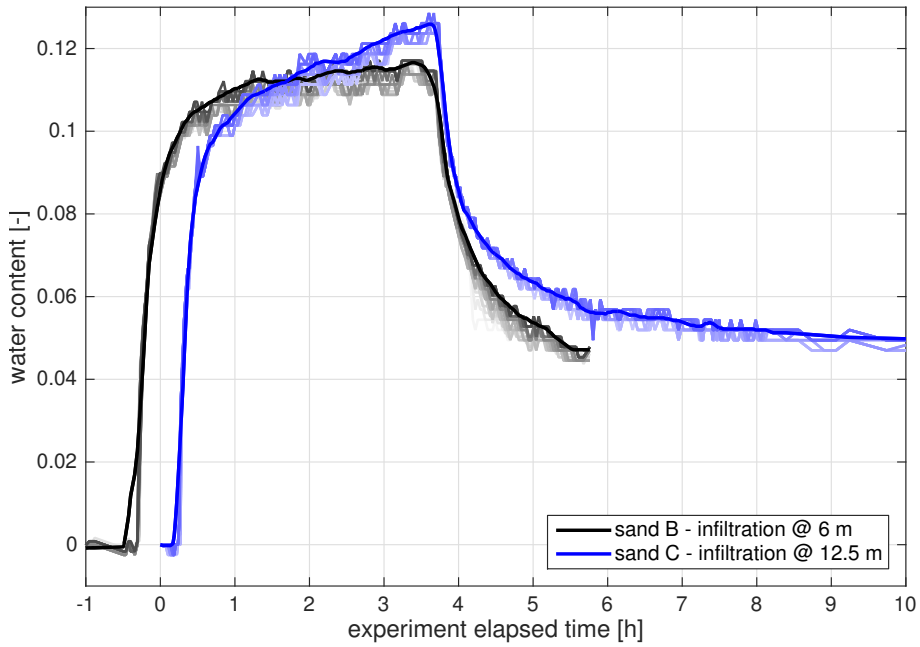

Figure 10. Soil water content variation over the course of the experiment averaged over 0.05 m around the respective centers of the two infiltration spots (solid blue and black lines, subjected to a ten minute run mean filter in time). The increasingly lighter blue and grey lines denote results if the traces are averaged over an increasingly larger spatial domain around the center of infiltration (up to ±1.3 m). For illustrative purposes, the time vector has been shifted to coincide at the end of the infiltration process.

HESSD
12, 12215–12246, 2015

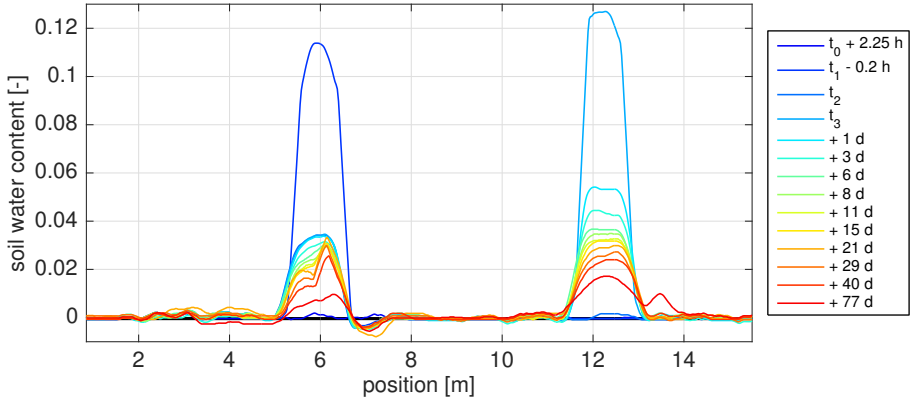

Figure 11. Longterm relaxation of the infiltration-induced water content variations evaluated from direct ground wave travel times as measured by CH1 at 600 MHz along the whole profile, passing the infiltration spots at 6 and 12.5 m, respectively. Between 6 and 6.5 m, the direct wave signal gets distorted after 10 days through an interference with a shallow material interface reflection. This distorted part has been excluded for calculating the mean values shown in Fig. 12.

HESSD
12, 12215–12246, 2015

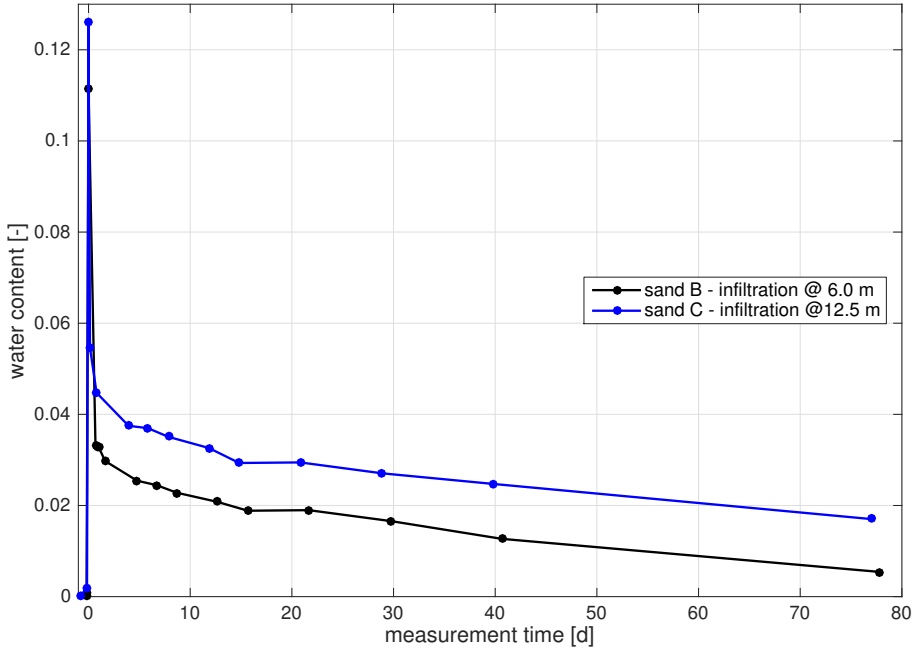

Figure 12. Comparison of peak water content, averaged over the center of the two infiltration spots. Throughout almost three months of relaxation, the coarser grained sand C (blue line) is consistently further from equilibrium than sand B (black line).

HESSD
12, 12215–12246, 2015